American Mineralogist, Volume 105, pages 1140–1151, 2020

Evaluation and application of the quartz-inclusions-in-epidote mineral barometer

Miguel Cisneros[1,2,*,†], Kyle T. Ashley[3], and Robert J. Bodnar[4]

[1]Current address: Structural Geology and Tectonics Group, Geological Institute, Department of Earth Sciences, ETH Zürich, Sonneggstrasse 5, Zürich, 8092, Switzerland

[2]Previous address: Department of Geological Sciences, Jackson School of Geosciences, University of Texas at Austin, 2275 Speedway Stop C9000, Austin, Texas 78712, U.S.A.

[3]Department of Geology and Environmental Science, University of Pittsburgh, 4107 O'Hara Street, Pittsburgh, Pennsylvania 15260, U.S.A.

[4]Department of Geosciences, Virginia Tech, 4044 Derring Hall (0420), Blacksburg, Virginia 24061, U.S.A.

Abstract

We have examined the suitability of a quartz-inclusions-in-epidote (qtz-in-ep) mineral barometer to better constrain *P-T* histories of epidote-bearing lithologies. Theoretical calculations applying an isotropic elastic model suggest that the qtz-in-ep barometer exhibits minimal temperature dependence, and thus, offers the potential to constrain growth conditions of epidote in various geologic environments, including skarn deposits, epidote-bearing granitoids, and metamorphic rocks.

To test if the applied equations of state and isotropic elastic model reasonably simulate the elastic evolution of two anisotropic minerals, we measured Raman shifts of the 464 cm^{-1} band of quartz inclusions relative to that of an unencapsulated quartz standard. We calculated a quartz inclusion pressure (P_{incl}^{464}) at various temperatures and compared these values with temperature-dependent P_{incl} predicted by elastic modeling (P_{incl}^{mod}) at elevated temperatures. Three epidote-bearing samples with reasonably well-constrained *P-T* histories were also examined: (1) sample HF14C from the Upper Schieferhuelle in the Western Tauern Window, Italy ($P_{incl}^{464} = 0.01$ GPa); (2) sample LdC-31C from Lago di Cignana, Italy ($P_{incl}^{464} \approx 0.16$ GPa); and (3) sample FT1E from the Frosnitz Tal in the Western Tauern region, Austria ($P_{incl}^{464} = 0.57$ GPa).

Entrapment pressures (P_{ent}^{464}) calculated from P_{incl}^{464} determined at various temperatures show nominal differences from P_{ent} calculated from P_{incl}^{mod}, suggesting that for qtz-in-ep pairs, the calculated P_{ent} does not significantly vary with the temperature of measurement. Furthermore, our calculated P_{ent}^{464} for a sample from the Upper Schieferhuelle is in agreement with petrographic context and previously established *P* conditions, and the P_{ent}^{464} determined for the Frosnitz Tal sample closely approximate previously reported pressures. The Lago di Cignana sample is derived from an epidote vein that is encased in a high-*P* foliation, and the calculated P_{ent}^{464} is consistent with early, low-*P* epidote vein formation that pre-dates high-*P* metamorphism, or alternatively, late vein formation during exhumation, and confirms that the epidote did not form at or near peak conditions (~2.0 GPa). The results of this study indicate that the qtz-in-ep barometer potentially provides another tool that geoscientists can employ to better constrain *P-T* conditions in some epidote-bearing environments, where conventional thermobarometric techniques cannot be applied.

Keywords: Elastic thermobarometry, epidote, Raman spectroscopy, quartz inclusions, thermobarometry; Applications of Fluid, Mineral, and Melt Inclusions

Introduction

A fundamental goal of many geosciences studies is to constrain the pressure-temperature (*P-T*) histories of igneous and metamorphic rocks. Many different thermobarometers have been developed during the past decades to unravel complex *P-T* histories, and in recent years, elastic thermobarometry has gained wide acceptance and applicability. Elastic thermobarometry is a method that can constrain *P-T* conditions in a wide range of geologic environments and records conditions at which a host crystal grows and encapsulates a mineral inclusion. Because the elastic properties of the inclusion and host almost always differ, upon exhumation an inclusion can develop a residual pressure that is higher (or lower) than that of the surrounding host. Application of elastic thermobarometers requires that changes in inclusion and host volumes from the time of host growth through exhumation to Earth's surface are well constrained. When combined with careful petrographic, mineralogical, and petrological studies, the method can be applied to constrain *P-T* conditions of mineral growth and fabric development, allowing deformation and tectonic processes to be independently constrained. The potential applications of the technique are many, yet the applicability of the technique has been limited to a few inclusion-host pairs, such as apatite-in-garnet (Ashley et al. 2017; Barkoff et al. 2017, 2019), quartz-in-garnet (e.g., Enami et al. 2007; Ashley et al. 2014, 2015; Kouketsu et al. 2014; Spear et al. 2014; Behr et al. 2018; Bonazzi et al. 2019), zircon-in-garnet (Zhong et al. 2019), garnet-in-diamond (Kueter et al. 2016), kyanite-in-diamond (Nestola et al. 2018), magnesiochromite-in-diamond (Nestola

* E-mail: miguel.cisneros@erdw.ethz.ch. Orcid 0000-0002-4884-4179.

† Special collection papers can be found online at http://www.minsocam.org/MSA/AmMin/special-collections.html.

0003-004X/20/0008–1140$05.00/DOI: https://doi.org/10.2138/am-2020-7379

et al. 2019), olivine-in-diamond (Izraeli et al. 1999; Nestola et al. 2011; Howell et al. 2012), periclase-in-diamond (Anzolini et al. 2019), and coesite-in-diamond, garnet, and zircon (Parkinson and Katayama 1999; Sobolev et al. 2000). The quartz-in-garnet (qtz-in-grt) inclusion-host pair is the most commonly implemented barometer because the high compressibility of quartz relative to the rigid host garnet allows for retention of significant residual pressures. Additionally, the ubiquity of quartz inclusions in garnet, the stability of garnet across a wide range of *P-T* conditions, and the fact that garnet is a nearly isotropic host makes this technique applicable to a wide range of geologic environments.

Quartz-in-epidote (qtz-in-ep) is similarly a potentially useful barometer because: (1) the qtz-in-ep barometer exhibits minimal temperature dependence (Fig. 1); (2) epidote is abundant and crystallizes in a broad range of geologic settings (*P-T* conditions); (3) quartz is commonly found as inclusions within epidote in a wide range of rock types; and (4) the thermodynamic properties of quartz and epidote group minerals are reasonably well constrained (e.g., Holland et al. 1996; Pawley et al. 1996; Mao et al. 2007; Gatta et al. 2011; Qin et al. 2016). The barometer is not limited by sluggish kinetics and partial disequilibrium (e.g., Rubie 1998; Carlson 2002), and can help to constrain *P-T* conditions that other thermobarometers may fail to record (e.g., fluid inclusions are commonly modified or destroyed during prograde metamorphism). The qtz-in-ep barometer offers the potential to constrain formation conditions in several environments for which few other barometers are available, including epidote-bearing skarn deposits, epidote-bearing granitoids, metamorphic rocks, epidote veins, and hydrothermally altered igneous rocks. The qtz-in-ep barometer, combined with detailed field observations, examination of microstructures and petrographic relationships, and independent thermobarometry, offers the possibility to considerably improve our understanding of the *P-T* history of epidote-bearing rocks. The qtz-in-ep barometer can potentially refine estimates of depths (pressures) of epidote formation in metamorphic rocks and can be applied to a wide range of bulk compositions, and the barometer can also supplement existing techniques to determine formation conditions of epidote-bearing granitoids and skarns.

This study describes the applicability of a qtz-in-ep barometer by measuring temperature-dependent Raman band positions of quartz, and comparing entrapment pressures calculated from elastic thermobarometry with independent thermobarometry (Selverstone and Spear 1985; Selverstone et al. 1992; Frezzotti et al. 2011). We follow a similar approach to that implemented by Ashley et al. (2016). Elastic models have been developed for isotropic minerals and assume a spherical inclusion geometry, and experiments that determine pressure-dependent Raman shifts are carried out under hydrostatic conditions. For the quartz-in-epidote pair, these assumptions may not be appropriate, necessitating the need for heating measurements to monitor the inclusion pressure of the inclusion-host pair as temperature changes. Therefore, Raman analyses were conducted at various temperatures to test the ability of the current modeling approach to predict the evolution of inclusion pressure during heating of two anisotropic minerals (quartz-in-epidote). We compare heating measurements and model results by two methods: (1) the Raman shift of the quartz 464 cm^{-1} band was measured and used to calculate an inclusion pressure (P^{464}_{incl}) at a given temperature, which we compared to P_{incl} that is predicted by elastic modeling at elevated temperatures (P^{mod}_{ent}), and (2) entrapment pressures (P^{464}_{ent}) are calculated based on P^{464}_{incl} at elevated temperature and are compared to entrapment pressures calculated from P^{mod}_{ent}.

Samples

Quartz inclusions in epidote from three samples with well-constrained *P-T* histories were analyzed, and we compared our pressure estimates to the previously determined *P-T* histories. The samples are from three different localities that have experienced different *P-T* histories, and they allow us to test the feasibility of implementing the qtz-in-ep barometer in metamorphic rocks that have experienced different *P-T* paths. We also consider whether our calculated entrapment pressures are reasonable and consistent with the petrographic evidence that documents the formation and deformation history of the epidote hosts.

Upper Schierferhuelle HF14C

Sample HF14C is a metamafic rock from the Upper Schieferhuelle (USH) in the Western Tauern Window, Italy, that contains a well-defined foliation defined by amphibole, epidote, quartz, chlorite, and plagioclase. *P-T* estimates that are used here for comparison have been derived from pelitic and mafic samples in the USH.

Reference *P-T* conditions of USH pelites have been estimated based on: (1) mineral chemistry thermobarometry; (2) Gibbs modeling of garnet zoning; and (3) fluid-inclusion thermobarometry (Ferry and Spear 1978; Spear and Selverstone 1983; Selverstone and Spear 1985). Garnet-biotite thermometry, and garnet-plagioclase-biotite-muscovite barometry (from garnet rims and matrix grain rims) give *P-T* estimates of ~475 ± 25 °C and ~0.5–0.6 GPa. Garnet core and rim modeling indicate *P-T* conditions of ~450 °C and ~0.5–0.6 GPa, and ~475 °C and ~0.5–0.6 GPa, respectively. Garnet zoning between cores and rims indicates intermittent pressure fluctuations during heating. The texturally oldest fluid inclusions in this sample indicate *P-T* conditions of ~0.6 GPa and ~450–500 °C and may record near peak (*T*) conditions or the early stages of USH exhumation. Younger fluid inclusions indicate near isothermal decompression after the USH reached peak *P-T* conditions.

P-T constraints for the mafic samples from the Upper Schieferhuelle (USH) are based on a lack of glaucophane, the presence of lawsonite pseudomorphs, and the stability of Ca-amphibole, albite, and chlorite throughout the history of the mafic samples, which places *P-T* conditions in a field that has been described as the lawsonite-albite-chlorite subfacies of blueschist facies (~0.4–0.6 GPa; Turner 1981; Selverstone and Spear 1985; Peacock 1993). Epidotes from this sample are oriented parallel to foliation and suggest that growth of epidote occurred prior to, or during, foliation-forming deformation (Fig. 2a)—this observation is important for comparing our results with previous *P-T* estimates, as described in more detail below.

Lago di Cignana LdC-31C

Sample LdC-31C (SESAR database; hand sample: IGSN = IECHL005C, thin section: IGSN = IECHL00B2) is a felsic rock from Lago di Cignana, Italy (Selverstone and Sharp 2013), a region that has experienced ultrahigh-pressure metamorphism as

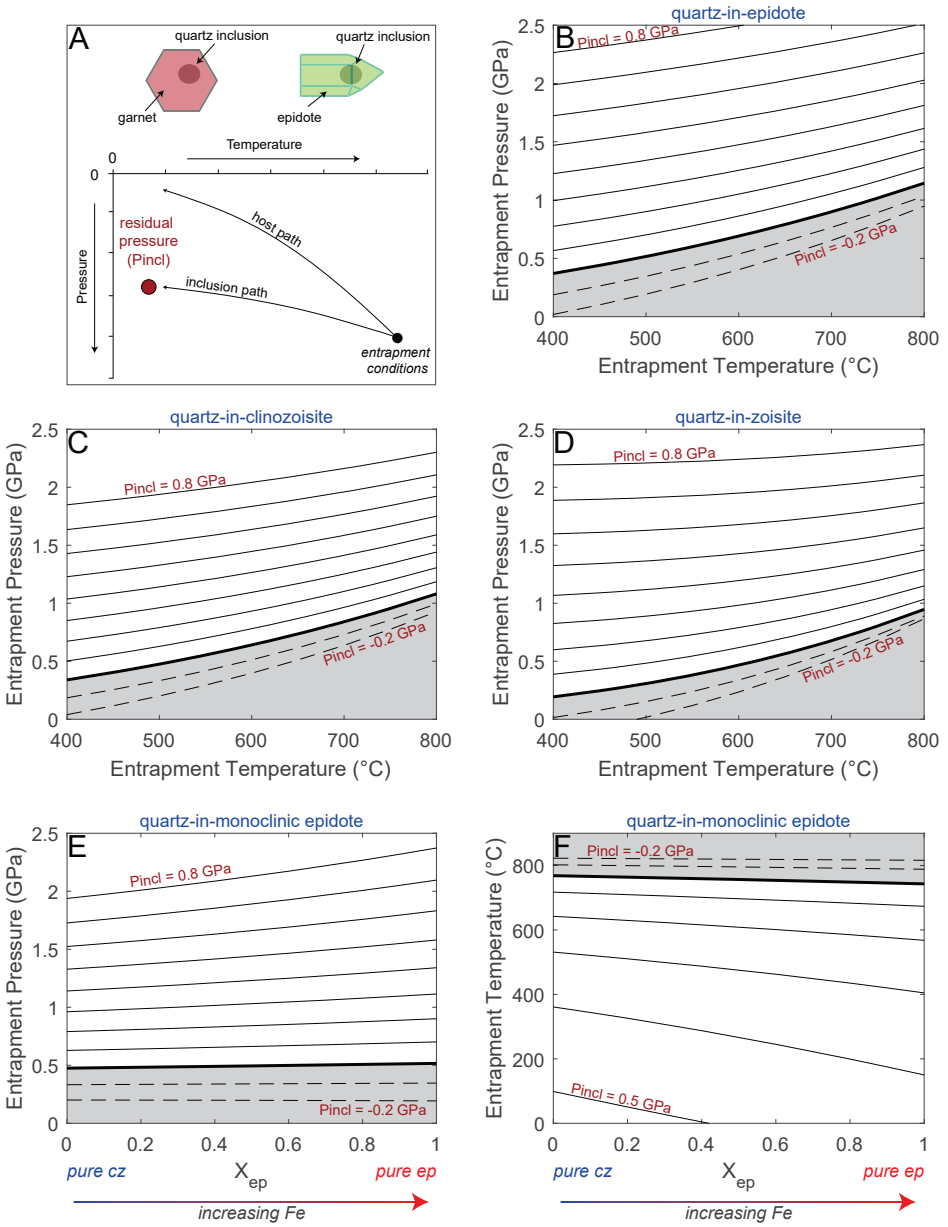

Figure 1. (**a**) Schematic illustration of the evolution of a host phase (e.g., epidote) and an inclusion (e.g., quartz) during exhumation, and the residual pressure (P_{incl}) retained by a quartz inclusion at ambient T (modified from Guiraud and Powell 2006; Befus et al. 2018). Models of the P-T dependence of P_{incl} for quartz in (**b**) epidote, (**c**) clinozoisite, and (**d**) zoisite. Models vary over the range of P_{incl} = –0.2 to 0.8 GPa (0.1 GPa intervals) and from 400–800 °C. Models show that P_{incl} is nominally affected by the assumed entrapment temperature. Dependence of entrapment pressure (**e**) and temperature (**f**) on the mole fraction (X_{ep}) of Al-Fe monoclinic epidote at T = 500 °C and P = 1 GPa, respectively. At low P_{incl}, the composition of epidote minimally affects the final entrapment pressure or temperature. At higher P_{incl}, the final entrapment pressure and temperature are more dependent on X_{ep}. Regions in gray denote conditions at which P_{incl} is below 0 GPa, wherein quartz preserves a tensile stress. (Color online.)

evidenced by a diamond-bearing horizon (Frezzotti et al. 2011). Temperature estimates of ~600 °C, with minimum pressure estimates of 3.2–3.4 GPa, suggest that these samples reached the diamond stability field where quartz is not stable (Groppo et al. 2009; Frezzotti et al. 2011). The foliation in the rock is defined by quartz, epidote, and white mica; however, epidote that we analyzed is derived from a coarse-grained epidote-fuchsite vein that exhibits an irregular, undulating contact with the primary foliation (Fig. 2b). The undulating boundary suggests that the epidote in the vein may have formed prior to the primary foliation-forming event in the region, or during exhumation, and experienced minor deformation after formation of the primary foliation.

Frosnitz Tal FT1E

Sample FT1E is a metasediment from Frosnitz Tal in the Tauern Window, Austria, that contains a well-defined foliation

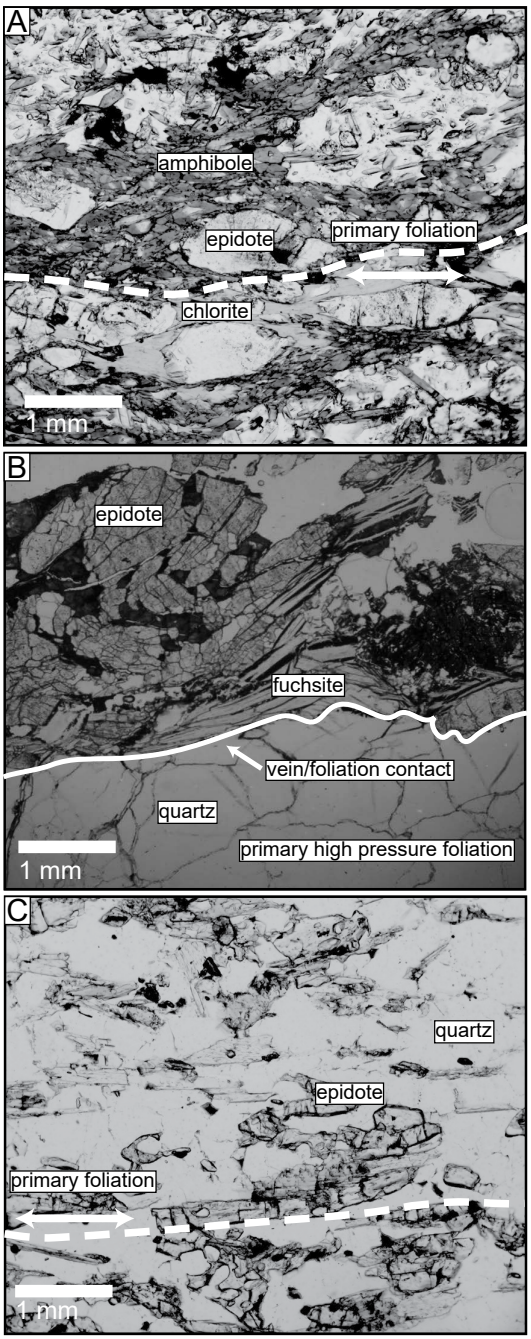

Figure 2. Photomicrographs of thin sections showing the petrographic relationships of epidotes analyzed in this study. (**a**) HF14C: foliation parallel epidote grains suggest that epidote likely grew prior to or during deformation associated with formation of the primary foliation. (**b**) LdC-31C: analyzed epidotes are from a vein that has an irregular, undulating contact with the primary foliation. The petrographic relations suggest that epidote crystallized prior to formation of the HP/LT foliation, or during exhumation. This fabric and the presence of quartz inclusions and lack of coesite suggests that the epidotes record formation pressures below high-pressure conditions where coesite is stable. (**c**) FT1E: epidote grains aligned parallel to foliation, suggesting that crystallization occurred prior to, or during, the formation of the primary foliation.

defined by quartz, epidote, white mica, omphacite, and chlorite (Fig. 2c). Most published *P-T* conditions for the area are derived from metabasites from the eclogite zone, and indicate peak metamorphic conditions of ~625 °C and ~1.9–2.5 GPa, based on multiple thermobarometric techniques, e.g., Holland (1979): 650 C, 1.95 GPa; Selverstone et al. (1992): 625 °C, 2.0 GPa; Kurz et al. (1998): 550–635 °C, 1.9–2.3 GPa; Hoschek (2001): 590–630 °C, 1.95–2.24 GPa; Miller and Konzett (2003): 623 °C, 2.04 GPa; Hoschek (2007): 630 °C, 2.5 GPa. Slightly lower peak *P-T* conditions ($P \approx 2.0$ GPa, $T \approx 600$ °C) have been estimated for adjacent metasediments (e.g., Spear and Franz 1986). Epidotes in the matrix are oriented parallel to the primary foliation, suggesting crystallization of epidote occurred prior to, or during, the primary fabric forming deformation.

Analytical methods

To test the suitability of using an isotropic elastic model to interpret data obtained from two anisotropic phases, quartz inclusions in epidotes from three localities were analyzed by Raman spectroscopy at various temperatures. For samples HF14C and FT1E, a single quartz inclusion in epidote was analyzed. During heating and analysis of a quartz inclusion in sample LdC-31C, the window in the heating stage cracked and the inclusion could not be heated to the final temperature; a second inclusion in a different epidote crystal from this sample was selected and analyzed. Samples were prepared by doubly polishing single epidote crystals that were then individually loaded onto a heating stage for Raman analyses. The diameter of measured quartz inclusions ranged from 10–15 μm, and significant care was taken to select isolated inclusions that were away from recognizable fractures, cleavage or other inclusions, and at least 3 times the inclusion radial distance from the host exterior (surface) to avoid relaxation of the inclusion (Campomenosi et al. 2018; Mazzucchelli et al. 2018).

Analyses during heating were completed at Virginia Tech on a Linkam THMSG600 heating stage mounted onto a JY Horiba LabRam HR800 Raman spectrometer with 1800 lines/mm grating. We used a 40x objective with a confocal aperture of 400 μm and a 150 μm slit width. Raman spectra were centered at 360 cm^{-1} (total spectral range of ~74–633 cm^{-1}). All spectra were collected with a 514.57 nm wavelength Ar laser, 30–45 s accumulation time, and 3 accumulations. The laser interference filter was removed for all analyses, allowing us to simultaneously correct measurements for drift by monitoring the position of the Ar plasma lines. For all samples, Raman analyses were performed at ambient pressure and from room temperature to 600 °C in 50 °C increments. The inclusions were also analyzed during subsequent cooling to test for reproducibility to ensure that the deformation induced during heating was elastic. All Raman spectra were temperature reduced using the Bose-Einstein distribution factor to compare Raman measurements made at elevated temperatures (Kuzmany 2009). After the spectra were temperature reduced, a linear background correction was applied to samples LdC-31C and HF14C, and a polynomial background correction was applied to sample FT1E (raw and reduced Raman spectra are provided in the Supplementary Material). All Raman data was fit using PeakFit v4.12 (by Systat Software Inc.). A Gaussian area model was used to fit Ar plasma lines, and a Voigt Gaussian/Lorentz area model was used to fit quartz and adjacent epidote bands. The 116.04, 266.29, and 520.3 cm^{-1} Ar plasma lines were used for linear drift corrections of the peak positions of quartz vibrational modes near 128, 206, and 464 cm^{-1}, respectively. Peak positions of quartz inclusion bands were determined relative to the peak positions of an unencapsulated Herkimer quartz standard that was analyzed five times every day during the analysis of the inclusions (Supplemental[1] Table S1). The propagated errors reported in this study account for errors in peak fit statistics for the Ar plasma line, quartz peaks, and instrumental uncertainty (±0.1 cm^{-1}).

Based on information in the RRUFF database (Lafuente et al. 2016), the Raman spectra of monoclinic epidotes show bands in the region from ~375–550 cm^{-1}. Epidotes have vibrational modes that exhibit strong Raman intensities at ~425 and 455 cm^{-1}, and lower intensity Raman modes at ~396, ~443, ~475, ~490, ~510, and ~528 cm^{-1}. The absolute band position and intensity varies depending on composition (Figs. 3a and 3b). Furthermore, the intensity of the epidote bands varies with crystal orientation, due to the orientation-dependent polarizability of mineral vibrational modes (Figs. 3a and 3b; Graves and Gardiner 1989). To account for peak overlap, we deconvolved Raman bands that are between ~375–550 cm^{-1} into ~10 peaks to simultaneously fit the quartz 464 cm^{-1} band,

adjacent epidote bands (~8 bands), and the 520.3 cm^{-1} Ar plasma line (Fig. 3, all high-*T* peak fits are provided in the Supplementary Material). The interference (overlap) of the quartz 464 cm^{-1} band with shouldering epidote bands becomes more pronounced at higher *T* as the quartz band shifts to lower wavenumbers and mineral peaks broaden. As epidote bands broadened at high temperature, some lower intensity bands became hidden, and they were removed from the peak fitting procedure due to the large uncertainty associated with their peak fit positions.

Electron probe microanalyses (EPMA) were carried out at the University of Texas at Austin on a JEOL 8200 microprobe equipped with five wavelength-dispersive spectrometers. Epidotes were analyzed for Na, Al, K, Mn, Ti, Mg, Si, Ca, Fe, and Cr using a 10 μm beam size, 10 nA beam current, and 15 keV accelerating voltage. All elements were measured for 30 s on peak and a mean atomic number background correction was applied. Primary standards used include: synthetic anorthite glass; synthetic orthoclase; natural chromite from the Stillwater complex (531M-8); synthetic enstatite; natural Amelia albite from Amelia, Virginia; and ilmenite from the Ilmen Mountains, USSR (USNM96189). Analyses were monitored by analyzing Kakanui hornblende as a secondary standard, using the same operating conditions as for the unknowns. All iron in epidote was assumed to be ferric, and epidotes were classified according to the nomenclature of Franz and Liebscher (2004). Major element compositions of epidote hosts in this study and the mole fractions of epidote components (epidote and clinozoisite) are given in Supplemental[1] Table S5.

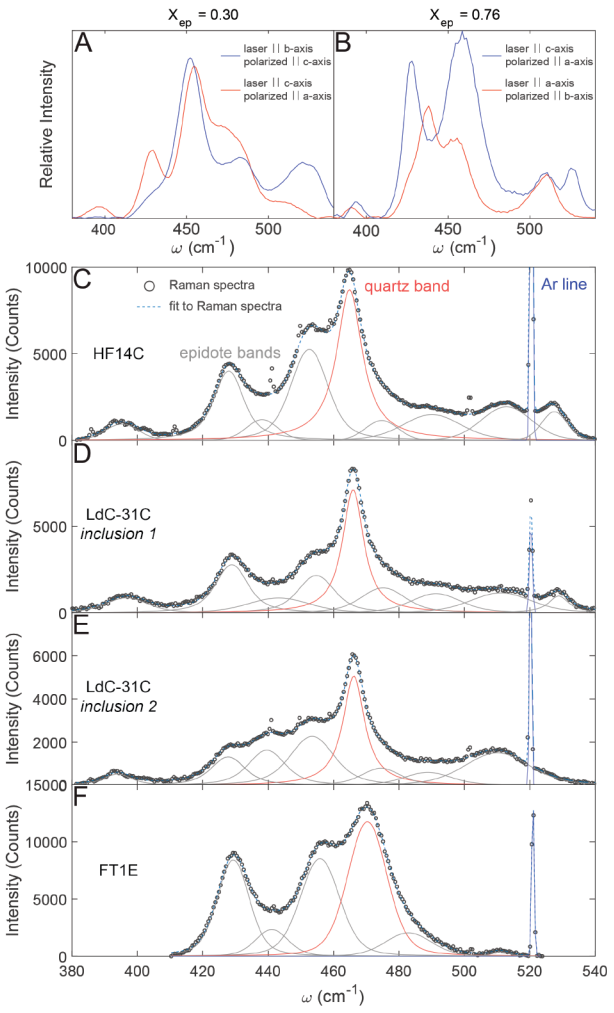

Figure 3. Raman spectra of epidotes (**a**) R060284 (X$_{ep}$ = 0.30) and (**b**) R050131 (X$_{ep}$ = 0.76) from the RRUFF database, and Raman spectra of all samples at ambient conditions and their associated peaks after fitting. (**a** and **b**) Raman spectra of epidotes are shown in two epidote orientations (red and blue lines) over the wavenumber region 380–540 cm^{-1}. (**c**, **d**, **e**, and **f**) shown in circles are the Raman spectra, the dashed blue line is the fit to the Raman spectra, and solid lines indicate the peaks used to fit the quartz 464 cm^{-1} band (red), epidote bands (gray), and the 520.3 cm^{-1} Ar-plasma line (blue). (Color online.)

Calculation procedures

Calculation of inclusion pressures

Raman shifts of the quartz (inclusion) 464 cm^{-1} band (ω^{464}_{incl}) at a given temperature were determined relative to the Raman shift of the 464 cm^{-1} band of a Herkimer quartz crystal (ω^{464}_{std}) measured at 0.1 MPa and the same temperature ($\Delta\omega^{464}_{shift} = \omega^{464}_{incl} - \omega^{464}_{std}$; definitions of abbreviations used here are listed in Table 1). This allowed us to correct for the temperature-induced strain on the quartz inclusions and to monitor stress-induced strains (Murri et al. 2018, 2019). For sample HF14C (low-*P* inclusion), we calculate $\Delta\omega^{464}_{shift}$ of inclusions relative to the Herkimer quartz standard using a polynomial equation that describes the ω^{464}_{std} of a Herkimer quartz analyzed at 0.1 MPa and the measurement temperature. The ω^{464}_{std}-temperature relationship is linear over most of the temperature range, but deviates from linearity near the quartz α-β transition (Fig. 4, Supplemental[1] Table S2, Ashley et al. 2016). The temperature of the quartz α-β transition occurs at ~573 °C at 0.1 MPa, and increases by about 0.25 °C/MPa. Thus, the higher P_{incl} samples (FT1E and LdC-31C) do not approach the quartz α-β transition during heating to 600 °C, and we calculated $\Delta\omega^{464}_{shift}$ using a linear extrapolation to the polynomial equation (Fig. 4, Supplemental[1] Table S3 and S4). Quartz inclusions in epidote record a smaller change in wavenumber of the 464 cm^{-1} Raman band during heating relative to Herkimer quartz at ambient pressure, because the inclusion pressure increases during heating. The increase in $\Delta\omega^{464}_{shift}$ reflects the effect of pressure on encapsulated quartz (inclusions) during heating, due to its higher thermal expansivity relative to epidote. The hydrostatic calibration of Schmidt and Ziemann (2000) was used to calculate P^{464}_{incl} from $\Delta\omega^{464}_{shift}$ at elevated *T*.

Recent studies report conflicting results concerning the accuracy of entrapment pressures that are calculated from Raman shifts of the quartz 464 cm^{-1} band with increasing pressure assuming hydrostatic calibrations (P^{464}_{incl}, Thomas and Spear 2018; Bonazzi et al. 2019). Some experiments that synthesize garnets with quartz inclusions show that P^{464}_{incl} provides accurate garnet growth pressures (Thomas and Spear 2018). Results from other experiments show that sometimes P^{464}_{incl} can accurately replicate experimental conditions (2.5 GPa experiments), but that in other cases (3.0 GPa experiments), use of the 464 cm^{-1} band underestimates experimental P_{ent}, and the use of quartz strains ($P^{strains}_{incl}$) better replicates experimental conditions (±0.2 GPa; Bonazzi et al. 2019). To assess the extent of anisotropy that quartz inclusions retain in an anisotropic host (epidote), we calculate $P^{strains}_{incl}$ to account for quartz anisotropy, and compare it to P_{incl} calculated from hydrostatic calibrations (Fig. 5, Supplemental[1] Table S2 and S3). Calculating quartz strains requires that Raman shifts of at least two quartz vibrational modes can be measured. For samples HF14C and LdC-31C, we measured the quartz 128, 206, and 464 cm^{-1} band positions at ambient temperature. Strains were determined from the Raman shifts of quartz 128, 206, and 464 cm^{-1} bands by using Strainman (Murri et al. 2018, 2019; Angel et al. 2019), and they were then converted to a mean stress [$P^{strains}_{incl} = (2\sigma_1 + \sigma_3)/3$] using the matrix relationship $\sigma_i = c_{ij}\varepsilon_j$, where σ_i, c_{ij}, and ε_j, are the stress, elastic modulus, and strain matrices, respectively. We used the α-quartz

Table 1. Abbreviations used in this manuscript

Abbreviation	Definition
ω^{464}_{std}	Wavenumber position of the quartz 464 cm^{-1} band of a standard at a measurement *T*.
ω^{464}_{incl}	Wavenumber position of the quartz 464 cm^{-1} band of an inclusion at a measurement *T*.
$\Delta\omega^{464}_{shift}$	$\Delta\omega^{464}_{shift} = \omega^{464}_{incl} - \omega^{464}_{std}$.
P^{128}_{incl}	Inclusion pressure calculated from the hydrostatic calibration of the quartz 128 cm^{-1} band.
P^{206}_{incl}	Inclusion pressure calculated from the hydrostatic calibration of the quartz 206 cm^{-1} band.
P^{464}_{incl}	Inclusion pressure calculated from the hydrostatic calibration of the quartz 464 cm^{-1} band.
$P^{strains}_{incl}$	Inclusion pressure calculated from strains.
P^{mod}_{incl}	Inclusion pressure predicted by elastic modeling (Fig. S1B).
P^{464}_{ent}	Entrapment pressure calculated from P^{464}_{incl}.
HF14C	Sample from Upper Schieferhuelle.
LdC-31C	Samples from Lago di Cignana.
FT1E	Sample from Frosnitz Tal.

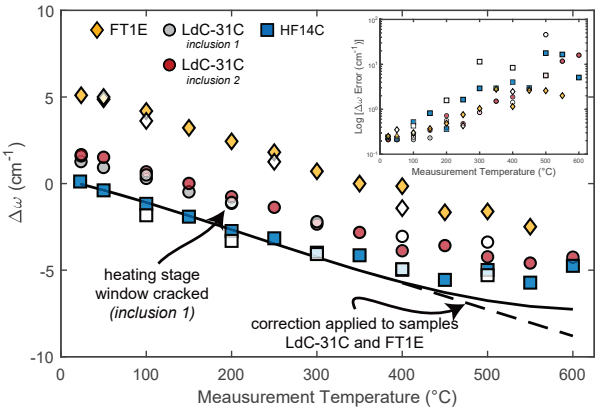

Figure 4. Raman shifts of the quartz (inclusion) 464 cm^{-1} band for the three samples measured during heating measurements. All samples display a decrease in wavenumber with increasing temperature. Relative to the position of the 464 cm^{-1} band of Herkimer quartz measured at ambient pressure, all inclusions exhibit a smaller change in the Raman shift of the quartz 464 cm^{-1} band due to an increase in inclusion pressure with increasing temperature. The solid black line is derived from the reference polynomial equation for the change in Raman shift of Herkimer quartz at 0.1 MPa and analysis *T* (Ashley et al. 2016). The dashed line is the linear extrapolation of the polynomial equation used to correct Raman shifts from samples LdC-31C and FT1E relative to Herkimer quartz at measurement conditions. Error bars are propagated errors from instrument uncertainty, and errors associated with fitting quartz 464 cm^{-1} bands and the Ar plasma line. Symbols represent the following samples: FT1E (yellow diamond), LdC-31C inclusion 1 (gray circle), LdC-31C inclusion 2 (red circle), HF14C (blue square). White (open) symbols represent measurements made during cooling. (Color online.)

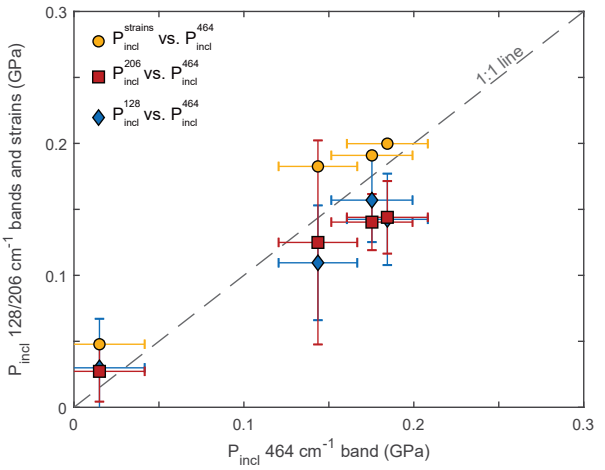

Figure 5. Comparison of P_{incl} calculated from the hydrostatic calibration of Raman shifts of quartz 128, 206, and 464 cm^{-1} bands, and P_{incl} calculated from strains. Yellow circles, red squares, and blue diamonds are the $P_{incl}^{strains}$ vs. P_{incl}^{464}, P_{incl}^{206} vs. P_{incl}^{464}, and P_{incl}^{128} vs. P_{incl}^{464} values, respectively. P_{incl} for sample LdC-31C (inclusion 2) is calculated at 23.7 and 23.8 °C. The dashed line shows where P_{incl} calculated from different bands and strains would have the same values (1:1 line). (Color online.)

trigonal symmetry constraints of Nye (1985) and quartz elastic constants of Wang et al. (2015). For sample FT1E, only the quartz 464 cm^{-1} band was fit at ambient temperature because the 128 and 206 cm^{-1} bands exhibited low intensities or had significant overlap with epidote peaks.

Calculation of entrapment conditions

Entrapment pressures (P_{ent}) and modeled inclusion pressures (P_{incl}^{mod}) were calculated by implementing the Guiraud and Powell (2006) 1D elastic model, with an updated exact solution described by Angel et al. (2017b), following the equation:

$$\left[\left(\frac{V_{P_{meas},T_{meas}}}{V_{P_{ent},T_{ent}}}\right)_{incl}-\left(\frac{V_{P_{meas},T_{meas}}}{V_{P_{ent},T_{ent}}}\right)_{host}\right]\left(\frac{V_{P_{ent},T_{ent}}}{V_{P_{foot},T_{meas}}}\right)_{incl}-\frac{3}{4G_{host}}\left(P_{incl}-P_{ext}\right)=0$$

where $(V_{P_{meas},T_{meas}}/V_{P_{ent},T_{ent}})_{incl}$ and $(V_{P_{meas},T_{meas}}/V_{P_{ent},T_{ent}})_{host}$ are the molar volume ratios of the entrapped inclusion and the host at measurement conditions ($V_{P_{meas},T_{meas}}$), and at entrapment conditions ($V_{P_{ent},T_{ent}}$), respectively. $(V_{P_{ent},T_{ent}}/V_{P_{meas},T_{meas}})_{incl}$ is the inclusion molar volume ratio at entrapment conditions, and at a measurement temperature and a pressure along an isomeke defined by the entrapment conditions (V_{Pfoot}, see Angel et al. 2017b). G_{host}, P_{incl}, and P_{ext} are the shear modulus of the host, the inclusion pressure at measurement conditions, and the pressure of the host (0.1 MPa) at ambient *T*, respectively. P_{incl}^{mod} and P_{ent} were calculated using an internal MATLAB script that allows for ideal mixing of solid-solutions; see Supplemental[1] Table S6 for a comparison of entrapment pressures calculated using EoSFit-*P*inc (Angel et al. 2017b). Modeled P_{incl} (P_{incl}^{mod}), i.e., the evolution of P_{incl} that is predicted by elastic modeling, is calculated by determining a residual quartz inclusion pressure (P_{incl}^{464}) at ambient *T* from Raman measurements, calculating an entrapment pressure (P_{ent}^{464}) from P_{incl}^{464} (and an assumed entrapment temperature), and subsequently back-calculating P_{incl}^{mod} at elevated *T* from the determined entrapment pressure (constant). Therefore, the modeled P_{ent} does not depend on the *T* of the Raman measurement. The increase of P_{incl}^{mod} reflects the increase in pressure that an inclusion would have to record at elevated *T* to predict the same P_{ent}. Entrapment pressures calculated from Raman measurements of quartz inclusions at elevated *T* (P_{ent}^{464}) use P_{incl}^{464} determined from quartz at various temperatures during heating of the sample, the *T* during heating measurements, and an assumed entrapment *T* (see Supplemental[1] Fig. S1 for a schematic illustration of the calculation method).

Molar volumes (*V*) of quartz were calculated using the quartz parameters of Angel et al. (2017a), and following their curved boundary model approach. Thermodynamic properties of epidote and clinozoisite were derived from the experimental *P-T-V* data of Gatta et al. (2011), and Qin et al. 2016 and Pawley et al. (1996), respectively. *P-T-V* data were fit using EoSFit7c (Angel et al. 2014). Epidote and clinozoisite data were fit with the modified Tait Equation of State (EoS) and thermal pressure term (Supplemental[1] Fig. S2). The clinozoisite thermodynamic properties are less well constrained, because the *P-T-V* data are derived from two experimental sources that used different epidote crystals [bulk modulus from Qin et al. (2016), X_{ep} = 0.39; thermal expansivity from Pawley et al. (1996), X_{ep} = 0.02]; therefore, the thermodynamic properties calculated using data from two different sources may have a larger uncertainty. The clinozoisite *P-V* data of Qin et al. (2016) were used because it shows smaller errors, and to the best of our knowledge, no updated *T-V* data exist for clinozoisite. For zoisite, we use the reference bulk modulus and thermal expansivity given in Holland and Powell (2011), and the Tait EoS and thermal pressure term (Table 2). Shear moduli for epidote, clinozoisite, and zoisite were calculated by implementing the aggregate Poisson's ratio of 0.26 from Mao et al. (2007) and the determined bulk moduli (Table 2). The shear modulus for an isotropic material is given by:

$$G=\frac{3K(1-2\nu)}{2(1+\nu)}$$

where *G* is the shear modulus, *K* is the bulk modulus, and ν is the Poisson ratio. This relationship predicts a shear modulus for epidote of 65.1 GPa, calculated from the Gatta et al. (2011) bulk modulus (Table 2); the calculated value closely approximates experimentally determined values (e.g., 61.2 GPa, Ryzhova et al. 1966). We are not aware of experimental shear modulus data for clinozoisite; therefore, to maintain internal consistency we calculate shear moduli using our regressed bulk moduli and Equation 2; the calculated shear moduli are given in Table 2. The small difference between experimentally derived and calculated shear moduli have a minimal effect on P_{ent}. The molar volume and shear modulus of epidote and clinozoisite solid-solution compositions were calculated assuming ideal (linear) mixing. A comparison of epidote *V*-X_{ep} (mole fraction of epidote) that is based on the compilation of Franz and Liebscher (2004) shows that linear mixing of molar volumes is an appropriate approximation (Supplemental[1] Fig. S3). Elastic modeling suggests that X_{ep} has a greater influence on calculated entrapment pressures when epidote preserves quartz with higher P_{incl} (Fig. 1d).

TABLE 2. Thermodynamic and physical properties of clinozoisite, epidote, and zoisite

Phase	V_0 (cm^3 mol^{-1})	α_0 (10^5 K^{-1})	κ_0 (GPa)	κ_0'	κ_0'' $\kappa_0'' = -\kappa_0'/\kappa_0$	S_0 [J/(mol·K)]	θ_E K	ν (Poisson ratio)	G (GPa)
Clinozoisite	138.1(4)[a]	2.24(6)[b]	147(2)[a]	4.0[a]	–0.027	301[e]	528.58	0.26[f]	84.0
Epidote	138.06(9)[c]	2.25(3)[c]	115(2)[c]	6.7(5)[c]	–0.058	315[e]	512.38	0.26[f]	65.7
Zoisite	135.80[d]	3.12[d]	104.4[d]	4.0[d]	–0.038	298[e]	532.19	0.26[f]	59.7

Notes: All thermodynamic properties are given at standard state: 0.1 MPa, 298 K. Einstein temperature (θ_E) is calculated from $\theta_E = 10636/(S_0/n_i + 6.44)$, where n_i is the number of atoms in epidote or zoisite (22). Reference *P-V-T* data from which thermodynamic properties are calculated:
[a] Qin et al. (2016) ($X_{Ep} = 0.39$), data fit with the Tait second-order EoS.
[b] Pawley et al. (1996) ($X_{Ep} = 0.02$), data fit with the Tait second-order EoS and thermal pressure.
[c] Gatta et al. (2011) ($X_{Ep} = 0.74$), data fit with the Tait third-order EoS and thermal pressure.
[d] Holland and Powell (2011), Tait second-order EoS and thermal pressure.
[e] References from which thermodynamic and physical properties are derived: Holland and Powell (2011).
[f] Mao et al. (2007).

RESULTS AND DISCUSSION

Raman analyses at ambient conditions

We compare P_{incl}^{464} of samples HF14C and LdC-31C with P_{incl} calculated from hydrostatic calibrations of Raman shifts of the 128 cm^{-1} (P_{incl}^{128}) and 206 cm^{-1} (P_{incl}^{206}) quartz bands with pressure (Schmidt and Ziemann 2000), and with strains ($P_{incl}^{strains}$). If we assume a $P_{incl}^{strains}$ error (1σ) that is equal to the error of P_{incl}^{464}, P_{incl} calculated from both approaches are within error (1σ, Fig. 5, Supplemental[1] Tables S2 and S3). We note that the $P_{incl}^{strains}$ error is a minimum uncertainty because the errors associated with peak fitting for the quartz 128 and 206 cm^{-1} bands are significant (Supplemental[1] Table S2 and S3).

P_{incl} estimates for sample HF14C resulting from hydrostatic calibrations of Raman shifts of quartz 128, 206, and 464 cm^{-1} bands are statistically identical (within error, 1σ): P_{incl}^{128} = 29 ± 37 MPa, P_{incl}^{206} = 27 ± 23 MPa, and P_{incl}^{464} = 15 ± 26 MPa (1σ, Fig. 5, Supplemental[1] Table S2). $P_{incl}^{strains}$ (48 MPa) indicates a slightly higher P_{incl} than that predicted from hydrostatic calibrations; however, the similar inclusion pressures calculated from hydrostatic calibrations and strains suggest that this quartz inclusion retains nominal strain anisotropy. Quartz inclusions from sample LdC-31C retain residual pressures of: P_{incl}^{128} = 90 ± 31 MPa, P_{incl}^{206} = 125 ± 77 MPa, P_{incl}^{464} = 144 ± 23 MPa (inclusion 1, 1σ) and P_{incl}^{128} = 157 ± 32 MPa, P_{incl}^{206} = 140 ± 21 MPa, P_{incl}^{464} = 175 ± 24 MPa (inclusion 2, 1σ). $P_{incl}^{strains}$ for both inclusions are slightly higher than predicted by the hydrostatic calibrations: $P_{incl}^{strains}$ = 183 MPa (inclusion 1) and $P_{incl}^{strains}$ = 191 MPa (inclusion 2) (Fig. 5, Supplemental[1] Table S3). LdC-31C inclusion 1 seems to record the largest anisotropy, as shown by the difference in inclusion pressures from hydrostatic calibrations. However, P_{incl}^{464} is within error of $P_{incl}^{strains}$ for all inclusions in samples HF14C and LdC-31C. The difference in P_{incl} calculated from P_{incl}^{464} and from strains results in a difference of <0.07 GPa in the final calculated entrapment pressure (Supplemental[1] Table S2 and S3).

We can further quantify the anisotropy of the α-quartz inclusions with trigonal symmetry ($\varepsilon_1 = \varepsilon_2$) by comparing strains that were determined from shifts of Raman band positions and the phonon-mode Grüneisen tensor, using the equation:

$$\Delta\varepsilon = \frac{\varepsilon_1 + \varepsilon_2}{2} - \varepsilon_3$$

The difference in strains (Δε) suggests that the HF14C quartz inclusion (Δε = –0.0017, Supplemental[1] Table S2) records anisotropy similar to LdC-31C inclusion 2 (inclusion 1: Δε = –0.0034, inclusion 2: Δε = –0.0013, Supplemental[1] Table S3). LdC-31C inclusion 1 records the largest anisotropy, but the limitations of using an isotropic elastic model and current EoS to predict the pressure evolution of this inclusion (P_{incl}^{mod}) showing greater anisotropy can only be evaluated up to 200 °C because the heating measurement was aborted when the window in the heating stage cracked (Fig. 4).

Raman analyses at elevated temperature

All quartz inclusions exhibited a shift of the 464 cm^{-1} band position to lower wavenumbers with increasing temperature, but encapsulated inclusions exhibit less of a shift compared to Raman bands of the Herkimer quartz standard analyzed at 0.1 MPa and the measurement temperature (Fig. 4). At elevated temperatures, we encountered difficulties in separating the quartz 464 cm^{-1} band and epidote shoulder bands due to their convergence that results from the *T*-dependence of Raman shifts and broadening of both the quartz and epidote bands with increasing temperature. The convergence of quartz and epidote bands caused a significant increase in peak fit errors, resulting in greater uncertainties associated with Δω, P_{incl}^{464}, and P_{ent}^{464} values at elevated *T* (Figs. 4, 6, and 7). At all temperatures, P_{incl}^{464} calculated from Raman measurements during heating and cooling are within error (1σ), and P_{incl}^{464} errors (1σ) exceed the difference between P_{incl}^{mod} (modeled) and P_{incl}^{464}; above 250 °C, peak fitting errors increase significantly (Figs. 6 and 7b). The increase in peak fit uncertainty makes it challenging to determine with confidence if the elastic model and associated EoS reproduce P_{incl}^{464} at elevated temperatures.

Samples HF14C and LdC-31C displayed the largest increase in P_{incl}^{464} during heating. The P_{incl}^{464} for sample HF14C is sufficiently low such that the quartz inclusion approaches the α-β transition during heating to 600 °C, and hence records a large increase in P_{incl}^{464}. P_{incl}^{464} calculated from measurements at elevated temperatures underestimated P_{incl}^{mod} significantly at low to moderate temperatures; however, the general trend of P_{incl}^{mod} is matched by P_{incl}^{464} at high temperatures (Fig. 6). Sample LdC-31C retains quartz inclusions with a higher P_{incl}^{464} such that during heating the α-β transition temperature is significantly higher than 600 °C and the trend is not influenced by the α-β transition. Nonetheless, quartz inclusion (#2) records the largest increase in P_{incl}^{464} that also matches the trend of P_{incl}^{mod}. P_{incl}^{464} calculated from LdC-31C inclusion 1 is within error of P_{incl}^{mod} up to the final measurement temperature at 200 °C. Sample FT1E exhibits the smallest increase in P_{incl}^{464} during heating, and P_{incl}^{464} calculated at super-ambient temperatures significantly underestimates P_{incl}^{mod} (Fig. 6). However, all P_{incl}^{464} values are within error (1σ) of P_{incl}^{mod}, owing to the high uncertainty associated with peak fits of sample FT1E.

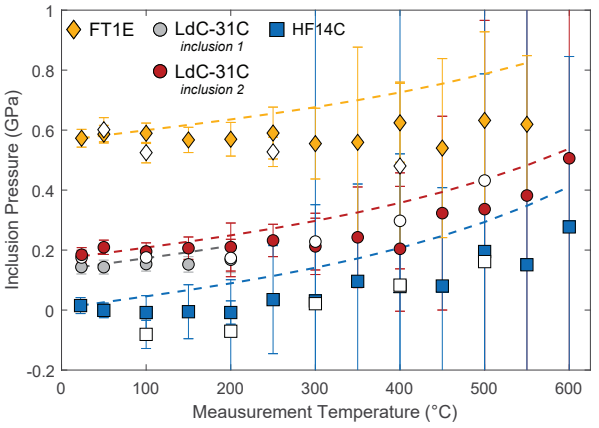

Figure 6. Inclusion pressures (P^{464}_{incl}) calculated from Raman analyses conducted during heating (symbols), compared to the P_{incl} evolution predicted by elastic modeling (P^{mod}_{incl}). The dashed lines represent P^{mod}_{incl}. P^{464}_{incl} errors (1σ) show the increase in error with increasing temperature. The error exceeds the difference between P^{464}_{incl} and P^{mod}_{incl}. Symbols represent the following samples: FT1E (yellow diamond), LdC-31C inclusion 1 (gray circle), LdC-31C inclusion 2 (red circle), HF14C (blue square). White (open) symbols are the measurements made during cooling. (Color online.)

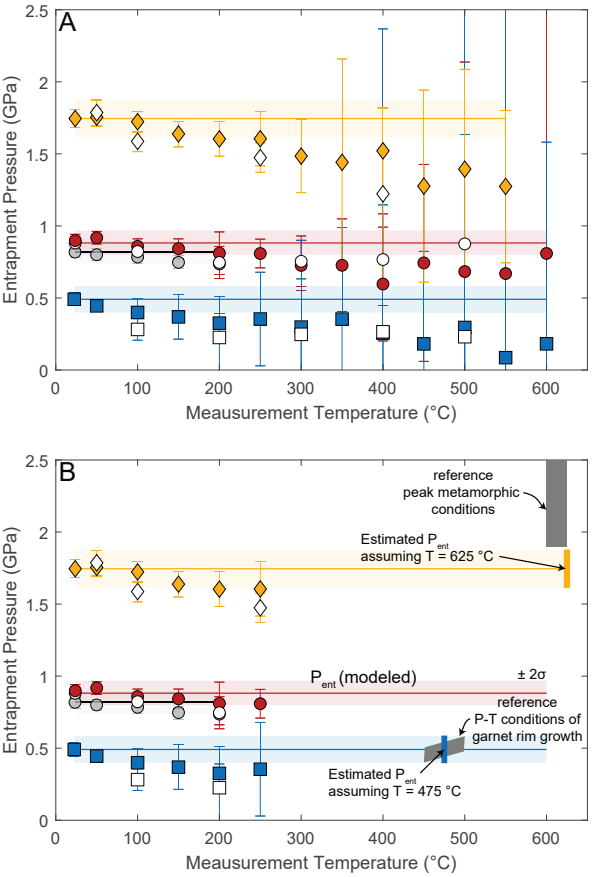

Figure 7. (**a**) Entrapment pressures calculated from P^{464}_{incl} determined from Raman shifts of quartz inclusions during heating (relative to a quartz crystal at 0.1 MPa and measurement *T*), and comparison with model estimates of the temperature-dependence of entrapment pressure (solid lines). Transparent colored lines bound errors of entrapment pressure estimates (±2σ). (**b**) Reference *P-T* conditions for samples FT1E and HF14C (gray boxes) and our estimated qtz-in-ep barometry entrapment pressures are shown for comparison. See text for discussion of the reference *P-T* conditions. Symbols represent the following samples: FT1E (yellow diamond), LdC-31C inclusion 1 (gray circle), LdC-31C inclusion 2 (red circle), HF14C (blue square). White (open) symbols represent measurements made during cooling. (Color online.)

The lower P^{464}_{incl} values obtained during heating likely reflect an overestimation of P^{mod}_{incl} by the elastic model and associated EoS, quartz anisotropy, measurement and peak fitting errors, or some combination of all of these factors; therefore, we do not use data from this inclusion to assess the reliability of the elastic model and EoS. It is possible that the quartz inclusion from sample FT1E records more anisotropic strain, or that the least thermally expansive axis of quartz is oriented parallel to the *c*-axis of epidote (maximum thermal expansivity), and therefore records a nominal pressure increase. Nonetheless, based on P^{464}_{incl} calculated from the lower temperature measurements of samples HF14C, LdC-31C, and FT1E (≤250 °C), our results suggest that application of the current equations of state, with an isotropic elastic model, satisfactorily simulates the evolution of P_{incl} with increasing temperature for anisotropic minerals (quartz and epidote).

Evaluation of calculated entrapment pressures at elevated temperatures

To evaluate the applicability of the elastic model and EoS for estimating entrapment pressures of quartz inclusions in epidote, we calculate entrapment pressures (P^{464}_{ent}) from P^{464}_{incl} derived at elevated temperatures (Fig. 7). Low P^{464}_{incl} sample HF14C showed the largest variation in calculated entrapment pressures, and measurements result in lower entrapment pressures relative to theoretical estimates at low temperatures. However, large uncertainties are associated with peak fits from sample HF14C due to the overlap of the quartz 464 cm^{-1} band with epidote shoulder bands, making peak deconvolution less robust. Likewise, sample FT1E exhibited a general decrease in P^{464}_{ent} with increasing *T*, but the quartz 464 cm^{-1} band exhibited a strong overlap with neighboring epidote bands at ambient and increasing *T* (Fig. 3f). Owing to these large uncertainties, it is challenging to use HF14C and FT1E data to evaluate whether entrapment pressure calculations require a thermal correction. We limit P^{464}_{ent} to $T \leq 250$ °C, a temperature at which most errors in P^{464}_{incl} are <0.1 GPa (Fig. 7a), to evaluate the need for a correction to P_{ent} calculated at elevated *T*. For these measurements, entrapment pressures calculated from P^{464}_{incl} of heated inclusions exhibit only small differences compared to entrapment pressures calculated from P^{mod}_{ent}. Most inclusions exhibit a decrease in absolute P^{464}_{ent} with increasing *T*, but all P^{464}_{ent} values remain within error (1σ) of modeled P_{ent}. We can also evaluate the difference between the mean P^{464}_{ent} of all Raman analyses of a single inclusion and P^{mod}_{ent}. We evaluate the weighted mean of Raman analyses of our analyzed inclusions by assigning a weight (ω_i) to each calculated P^{464}_{ent} that considers measurement uncertainty:

$$\omega_i = 1/\sigma_i^2$$

where σ_i is the 1σ error of each P_{ent}^{464} calculation (Supplemental[1] Tables S2, S3, and S4). For samples HF14C, LdC-31C, and FT1E, we calculate P_{ent}^{464} weighted means of 0.41, 0.79 and 0.86 GPa, and 1.67 GPa, respectively. These values slightly underestimate, but closely approximate, calculated P_{ent}^{mod} values of 0.49 GPa, 0.82 and 0.87 GPa, and 1.75 GPa, respectively. These observations suggest that the errors introduced by associated EoS, an isotropic elastic model, and Grüneisen tensor components are minimal and that the calculated entrapment pressure is not a function of the temperature at which the sample is analyzed (Fig. 7).

Comparison of calculated entrapment pressures to previously reported *P-T* histories

To assess if the quartz-in-epidote barometer provides reasonable estimates of the pressure of epidote growth, we compare our results to previously determined *P-T* conditions for our samples.

Upper Schierferhuelle Sample HF14C

Sample HF14C preserves foliation parallel epidotes that appear to have crystallized pre-or-syn-kinematic to fabric-forming deformation (Fig. 2a). Development of the dominant foliation (S1) observed in the mafic sample is proposed to have occurred early in the metamorphic history of the USH. This foliation was overprinted by static lawsonite growth in the mafic samples, and at least some of the epidote is associated with subsequent breakdown of lawsonite. A subsequent shear foliation subparallel to S1 is evident in the pelites, but not in the mafic rocks at the sample localities (Selverstone 1985). Garnet growth in pelites occurred after lawsonite breakdown, and rotated garnets indicate that they formed during development of the subparallel shear foliation (S1, Selverstone 1985). Epidote inclusions are found within garnets that formed near peak *T*. It is thus likely that matrix epidote analyzed in the mafic sample formed early, before USH rocks reach peak *T*. The epidote analyzed from this sample encapsulates a quartz inclusion with a residual $P_{incl}^{464} = 15 \pm 26$ (1σ) MPa, or $P_{incl}^{strains} = 48$ MPa. Assuming an entrapment temperature of 475 °C (below peak *T* of ~500 °C), we estimate entrapment pressures of 0.49 ± 0.10 (2σ) GPa from P_{incl}^{464}, and 0.55 GPa from $P_{incl}^{strains}$ (Fig. 7a, Supplemental[1] Table S2). These *P-T* estimates likely reflect epidote growth conditions prior to reaching peak *T* conditions, and our results are consistent with petrographic observations and previously established *P-T* constraints; these previous *P-T* constraints are derived from a range of thermobarometry approaches that give consistent results related to the *P-T* evolution of these samples [cation thermobarometry, Gibbs garnet modeling, and fluid inclusion thermobarometry; Selverstone and Spear (1985)]. It is possible that overstepping of reaction boundaries occurred during formation of epidotes, but the agreement of our results with petrographic constraints and independent thermobarometry suggest that overstepping did not significantly affect the *P-T* estimates obtained here.

Lago di Cignana Sample LdC-31C

Quartz inclusions 1 and 2 from sample LdC-31C retain residual pressures of $P_{incl}^{464} = 143 \pm 23$ (1σ) MPa and $P_{incl}^{464} = 175 \pm 24$ (1σ) MPa, or $P_{incl}^{strains} = 183$ MPa and $P_{incl}^{strains} = 191$ MPa, respectively. Assuming an entrapment temperature of 550 °C, we calculate an entrapment pressure of ~0.8–0.9 ± 0.08 (2σ) GPa (Fig. 7a, Supplemental[1] Table S3). This estimate is much lower than the reported peak metamorphic conditions of ~600 °C and 3.2–3.4 GPa (within the diamond-bearing horizon at Lago di Cignana; Frezzotti et al. 2011). However, the presence of quartz inclusions in epidote is clear evidence that the qtz-in-ep entrapment pressures do not record peak pressure conditions, where coesite is stable. Our calculated entrapment pressures, and field and petrographic relationships of epidote-fuchsite veins encased in the high-*P* foliation, suggests that epidote growth represents an early vein formation stage that predates HP/LT metamorphism in the Lago Di Cignana region or, alternatively, that the late epidote vein formed during exhumation and experienced only minor deformation (Fig. 2b). Our *P-T* estimates for sample LdC-31C are also consistent with retrograde metamorphic conditions that have been suggested by van der Klauw et al. (1997) (T = 550–500 °C, $P \approx 1.8$ GPa; T = 350–450 °C, $P \approx 0.35$–0.55 GPa); however, our samples show no evidence for extensive retrogression as represented by the preservation of HP assemblages. It is most likely that the epidote vein formed during exhumation and after leaving the coesite-stable field. If the epidote veins formed along the prograde path and before reaching peak conditions, the epidotes would have encapsulated quartz and would traverse through the coesite-stable field at peak conditions and then return to the quartz-stable region during exhumation. The preservation of quartz inclusions in these epidotes would require kinetic barriers to prevent formation of coesite at peak conditions or, conversely, mass conversion of coesite back to quartz along the retrograde path. While this scenario is possible, it is more likely that the epidote formed late, during exhumation and while *P-T* conditions were in the quartz stable field.

Frosnitz Tal Sample FT1E

Epidotes in sample FT1E are aligned parallel to the primary foliation, suggesting pre-to syn-tectonic crystallization of epidote (Fig. 2c). The quartz inclusion analyzed from sample FT1E retains a residual inclusion pressure of $P_{incl}^{464} = 573 \pm 30$ (1σ) MPa. Assuming an entrapment temperature of 625 °C, our results suggest a formation pressure of 1.75 ± 0.12 (2σ) GPa (Fig. 7a). Our predicted pressure is slightly lower than previous peak *P-T* estimates for the Frosnitz Tal eclogite zone in the Tauern Window ($T \approx 600$ °C, $P \approx 1.9$–2.5 GPa) (e.g., Spear and Franz 1986; Selverstone et al. 1992). Epidote growth conditions are further constrained by petrographic observations. Banded eclogites from the Frosnitz Tal contain epidote-zoisite pairs in apparent textural equilibrium, suggesting a transformation loop at ~2.0 GPa, 625 °C (Selverstone et al. 1992). Pseudosection models of banded eclogites from Eissee (Tauern Window eclogite zone) predict growth of matrix zoisite during exhumation at *P-T* conditions below ~1.9 GPa and ~625 °C (Hoschek 2007); however, pseudosections based on samples that have different bulk rock compositions should be compared with caution.

Corrections to the thermal component of the elastic model

The agreement between P_{incl}^{464} (measured) and P_{incl}^{mod} (P_{incl} predicted by elastic modeling) at $T \leq 250$ °C tentatively suggests that entrapment pressures calculated from the quartz-in-epidote barometer do not require a temperature-dependent correction; i.e., an empirical correction to entrapment pressures (based

on the estimated entrapment temperature) that accounts for elastic modeling or EoS errors, is not required. We note that at $T > 250$ °C, it is more difficult to evaluate the current elastic modeling approach and associated EoS, and our interpretation is limited by errors associated with fitting of the quartz 464 cm^{-1} band at elevated T. Our interpretation is consistent with results from the apatite-in-garnet barometer that conclude that a temperature correction is not needed for apatite inclusion pressure measurements conducted at ambient temperature and that are subsequently used to calculate entrapment pressures at higher temperatures (Ashley et al. 2017). In comparison, previous work suggests that a temperature correction is required for the qtz-in-grt barometer when the Raman 464 cm^{-1} band is used for inclusion P determination (Ashley et al. 2016). These somewhat contradictory results (i.e., no observed offset in measured and modeled inclusion P at elevated temperatures) are problematic, given that quartz is the common inclusion phase between the qtz-in-grt and qtz-in-ep barometers. P_{incl} estimates based on different quartz inclusion bands and strains are similar in this study and hence, the P_{incl}^{464} and P_{incl}^{mod} are similar, but significant disparities in pressures obtained from the different bands are observed for quartz in garnet, suggesting significant anisotropy (Bonazzi et al. 2019). Perhaps the lower bulk modulus of epidote results in a smaller stress anisotropy for the quartz inclusion that is not detectable with current methods. Additionally, because quartz and epidote typically (re)crystallize along a schistosity during fabric development, it may be that the orientation of the quartz inclusion relative to the epidote host leads to a bulk stress tensor that optimally characterizes the inclusion P for the system, and in this case, the mutual orientation of quartz inclusions in epidote minimizes quartz anisotropy due to the anisotropic expansion of epidote during heating (Gatta et al. 2011). Furthermore, the quartz inclusion in sample FT1E may record the largest anisotropy and the deviation of absolute values of P_{ent}^{464} from modeled P_{ent} may be real, but we cannot fully evaluate the extent of anisotropy preserved by this quartz inclusion. Regardless of the mechanism, our results lead to the following conclusions: (1) inclusion pressures calculated from the hydrostatic calibration of the quartz 464 cm^{-1} Raman band shifts (not valid for high anisotropic strain), yield nearly constant entrapment pressures (within uncertainty), independent of the temperature at which the inclusion is analyzed; and (2) allowing for errors introduced by modeling of entrapment pressures, our results suggest that the 1D-isotropic model is appropriate for modeling the elastic behavior of these two anisotropic phases, and no further correction is required for calculation of final entrapment pressures.

Quartz-in-epidote barometry limitations

A major limitation of the quartz-in-epidote barometer is related to the convergence of the 464 cm^{-1} Raman band of quartz (and other quartz bands) and the epidote shoulder bands as temperature is increased, causing peak overlap and requiring deconvolution to fit the quartz band. However, robust peak fits can be applied to most standard Raman measurements made at ambient T, wherein the peak overlap is less significant because the separation between the quartz 464 cm^{-1} band and epidote shoulder bands is larger. Elastic thermobarometry requires robust determination of positions of multiple bands to calculate strains and to account for anisotropy (Murri et al. 2018, 2019; Angel et al. 2019); however, epidotes contain many bands that overlap with quartz bands, especially those near 128, 206, and 464 cm^{-1}. To minimize uncertainties associated with fitting quartz peaks, sufficiently high quartz inclusion Raman intensities may be achieved by rotating samples to analyze quartz inclusions in different orientations. Different epidote and quartz bands will reach maximum intensities at different orientations due to the orientation-dependent polarizability of mineral vibrational modes (Raman band positions will not change), but an orientation that makes the quartz Raman bands dominant can minimize peak fitting uncertainties. Additionally, the Raman spectra of epidotes may be subtracted from the convolved Raman spectra of quartz and epidote to obtain a pure quartz Raman spectrum, but this would require careful evaluation. Choosing samples from high-P rocks that preserve quartz with high residual P_{incl}, may also limit overlap of quartz bands (e.g., 464 cm^{-1}) with high intensity epidote bands near ~425 and 455 cm^{-1}. For high-T/low-P samples, convergence of the 464 cm^{-1} quartz band may not allow separation of the quartz and epidote bands via deconvolution, perhaps limiting application of qtz-in-ep barometry to epidote crystals that have entrapped quartz under moderate to high pressure conditions. Further analyses using epidotes from magmatic systems or skarns that have well constrained P-T histories might help better understand the limitations of the technique.

We emphasize that our approach does not allow us to fully evaluate the reliability of the calculated entrapment pressures because we cannot demonstrate that reactions that produce epidote were not significantly overstepped. The importance of overstepping will depend on the relationship of the qtz-in-ep isomekes and the slope (dP/dT) of the epidote-in reaction line. Because qtz-in-ep isomekes are nearly flat, if the epidote-in reaction line is flat ($dP/dT = 0$) or vertical ($dT/dP = 0$), the effect of T is minimal. Between these extremes overstepping may become important, and will depend on the relative slopes of the qtz-in-ep isomekes and reaction line, and the P-T path of the rock. Furthermore, we cannot unambiguously determine if the final P_{ent}^{464} of sample FT1E is affected by quartz anisotropy; therefore, we advise that the uncertainties that we report for the entrapment pressures below be applied with caution. In spite of these concerns, the relatively good correlation between pressure determined here and P-T estimates and petrographic, field, and petrologic studies of the same areas provides confidence that the qtz-in-ep barometer provides reasonable pressure estimates in some cases. Future recommended studies would include comparing qtz-in-ep pressure estimates with additional samples that have good field, petrographic, and independent thermobarometry constraints, with modeled reactions that include both epidote and quartz as product phases, and/or synthesis experiments of quartz inclusions in epidote (e.g., Thomas and Spear 2018; Bonazzi et al. 2019).

Final comments and implications

This work highlights the potential of the qtz-in-ep barometer to constrain formation conditions of epidote, and also highlights some of the obstacles and uncertainties associated with implementing this barometer. The qtz-in-ep barometer was evaluated for moderate to high-P metamorphic rocks, but can potentially be applied to understand formation conditions of other geologic

processes that include epidote-bearing skarn formation, epidote growth in ore deposits, epidote-bearing granitoid rocks, hydrothermal alteration of oceanic crust, and growth conditions of epidote in metamorphic rocks from convergent margins. Although entrapment pressures calculated from the qtz-in-ep barometer are in general consistent with previous estimates for the samples studied, further work is needed to document the accuracy and reliability of entrapment pressures (e.g., synthesis experiments, or detailed petrographic studies that integrate reaction modeling). Nevertheless, qtz-in-ep entrapment pressures of samples from the Frosnitz Tal eclogite zone in the Tauern Window and the Upper Schieferhuelle in the Western Tauern are in general agreement with previously established *P-T* conditions. Qtz-in-ep entrapment pressures of samples from Lago di Cignana indicate vein epidote crystallization below the maximum pressure conditions of the area (diamond stability field). The presence of quartz inclusions suggests that the qtz-in-ep barometer records *P-T* conditions that are not in the diamond stability field, due to the lack of coesite, and highlights how field and petrographic observations can be combined with the barometer to better constrain cryptic stages of *P-T* histories. Furthermore, the results of our analyses at various temperatures suggest that a temperature-dependent entrapment pressure correction is not required, contrary to what has been noted for the qtz-in-grt barometer. Therefore, this work suggests that Raman measurements of quartz inclusions in epidote taken at ambient conditions can be used to calculate high-temperature entrapment pressures without applying temperature corrections (for quartz inclusions preserving near isotropic strains). Our results further highlight the importance of integrating data from mineral geobarometers with field and petrographic observations that document the relative timing of various mineral formation and deformation events to constrain *P-T* conditions associated with the development of distinct structural and textural fabrics.

Acknowledgments

The authors thank J. Selverstone for providing the reference samples used in this study and for informal reviews, M. Alvaro and R. Angel for help with evaluating *P-T-V* data, M. Murri and N. Campomenosi for discussions about Raman data reduction, and M. Mazzuchelli and M Gilio for helpful manuscript comments. We thank C. Cannatelli and D. Baker for editorial handling, and F. Spear and an anonymous reviewer for constructive reviews that greatly improved this manuscript. We thank T. Holland for assistance with modeling quartz volumes and Charles Farley for assistance with use of the Raman microprobe at Virginia Tech.

Funding

This work was supported by a Geological Society of America Student Research Grant and a Ford Foundation Fellowship awarded to M.C., and National Science Foundation Grants (EAR-1725110) awarded to J. Barnes, W. Behr, and D. Stockli, and to R.B. (EAR-1624589).

References cited

Angel, R.J., Alvaro, M., and Gonzalez-Platas, J. (2014) EosFit7c and a Fortran module (library) for equation of state calculations. Zeitschrift für Kristallographie Crystalline Materials, 229, 405–419.

Angel, R.J., Alvaro, M., Miletich, R., and Nestola, F. (2017a) A simple and generalised *P-T-V* EoS for continuous phase transitions, implemented in EosFit and applied to quartz. Contributions to Mineralogy and Petrology, 172, 29.

Angel, R.J., Mazzucchelli, M.L., Alvaro, M., and Nestola, F. (2017b) EosFit-Pinc: A simple GUI for host-inclusion elastic thermobarometry. American Mineralogist, 102, 1957–1960.

Angel, R.J., Murri, M., Mihailova, B., and Alvaro, M. (2019) Stress, strain and Raman shifts. Zeitschrift für Kristallographie Crystalline Materials, 234, 129–140.

Anzolini, C., Nestola, F., Mazzucchelli, M.L., Alvaro, M., Nimis, P., Gianese, A., Morganti, S., Marone, F., Campione, M., Hutchison, M.T., and others (2019) Depth of diamond formation obtained from single periclase inclusions. Geology, 47, 219–222.

Ashley, K.T., Caddick, M.J., Steele-MacInnis, M.J., Bodnar, R.J., and Dragovic, B. (2014) Geothermobarometric history of subduction recorded by quartz inclusions in garnet. Geochemistry, Geophysics, Geosystems, 15, 350–360.

Ashley, K.T., Darling, R.S., Bodnar, R.J., and Law, R.D. (2015) Significance of "stretched" mineral inclusions for reconstructing *P-T* exhumation history. Contributions to Mineralogy and Petrology, 169, 55.

Ashley, K.T., Steele-MacInnis, M., Bodnar, R.J., and Darling, R.S. (2016) Quartz-in-garnet inclusion barometry under fire: Reducing uncertainty from model estimates. Geology, 44, 699–702.

Ashley, K.T., Barkoff, D.W., and Steele-MacInnis, M. (2017) Barometric constraints based on apatite inclusions in garnet. American Mineralogist, 102, 743–749.

Barkoff, D.W., Ashley, K.T., and Steele-MacInnis, M. (2017) Pressures of skarn mineralization at Casting Copper, Nevada, U.S.A., based on apatite inclusions in garnet. Geology, 45, 947–950.

Barkoff, D.W., Ashley, K.T., Silva, R.G.D., Mazdab, F.K., and Steele-MacInnis, M. (2019) Thermobarometry of three skarns in the Ludwig Area, Nevada, Based on Raman spectroscopy and elastic modeling of mineral inclusions in garnet. Canadian Mineralogist, 57, 25–45.

Befus, K.S., Lin, J.-F., Cisneros, M., and Fu, S. (2018) Feldspar Raman shift and application as a magmatic thermobarometer. American Mineralogist, 103, 600–609.

Behr, W.M., Kotowski, A.J., and Ashley, K.T. (2018) Dehydration-induced rheological heterogeneity and the deep tremor source in warm subduction zones. Geology, 46, 475–478.

Bonazzi, P., and Menchetti, S. (1995) Monoclinic members of the epidote group: effects of the Al ⇌ Fe^{3+} ⇌ Fe^{2+} substitution and of the entry of REE^{3+}. Mineralogy and Petrology, 53, 133–153.

Bonazzi, M., Tumiati, S., Thomas, J., Angel, R.J., and Alvaro, M. (2019) Assessment of the reliability of elastic geobarometry with quartz inclusions. Lithos, 105201.

Campomenosi, N., Mazzucchelli, M.L., Mihailova, B., Scambelluri, M., Angel, R.J., Nestola, F., Reali, A., and Alvaro, M. (2018) How geometry and anisotropy affect residual strain in host-inclusion systems: Coupling experimental and numerical approaches. American Mineralogist, 103, 2032–2035.

Carbonin, S., and Molin, G. (1980) Crystal-chemical considerations on eight metamorphic epidotes. Neues Jahrbuch für Mineralogie (Abhandlungen), 139, 205–215.

Carlson, W.D. (2002) Scales of disequilibrium and rates of equilibration during metamorphism. American Mineralogist, 87, 185–204.

Comodi, P., and Zanazzi, P.F. (1997) The pressure behavior of clinozoisite and zoisite: An X-ray diffraction study. American Mineralogist, 82, 61–68.

Da-Wei, F., Mai-Ning, M., Jun-Jie, Y., Shu-Yi, W., Zhi-Qiang, C., and Hong-Sen, X. (2011) In situ high-pressure synchrotron X-ray diffraction study of clinozoisite. Chinese Physics Letters, 28, 126103.

Enami, M., Nishiyama, T., and Mouri, T. (2007) Laser Raman microspectrometry of metamorphic quartz: A simple method for comparison of metamorphic pressures. American Mineralogist, 92, 1303–1315.

Ferry, J.M., and Spear, F.S. (1978) Experimental calibration of the partitioning of Fe and Mg between biotite and garnet. Contributions to Mineralogy and Petrology, 66, 113–117.

Franz, G., and Liebscher, A. (2004) Physical and Chemical Properties of the Epidote Minerals–An Introduction. Reviews in Mineralogy and Geochemistry, 56, 1–81.

Frezzotti, M.L., Selverstone, J., Sharp, Z.D., and Compagnoni, R. (2011) Carbonate dissolution during subduction revealed by diamond-bearing rocks from the Alps. Nature Geoscience, 4, 703–706.

Gatta, G.D., Merlini, M., Lee, Y., and Poli, S. (2011) Behavior of epidote at high pressure and high temperature: a powder diffraction study up to 10 GPa and 1,200 K. Physics and Chemistry of Minerals, 38, 419–428.

Graves, P., and Gardiner, D. (1989) Practical Raman spectroscopy. Springer.

Groppo, C., Beltrando, M., and Compagnoni, R. (2009) The *P-T* path of the ultra-high pressure Lago Di Cignana and adjoining high-pressure meta-ophiolitic units: insights into the evolution of the subducting Tethyan slab. Journal of Metamorphic Geology, 27, 207–231.

Giuli, G., Bonazzi, P., and Menchetti, S. (2015) Al-Fe disorder in synthetic epidotes: A single-crystal X-ray diffraction study. American Mineralogist, 84, 933–936.

Guiraud, M., and Powell, R. (2006) *P-V-T* relationships and mineral equilibria in inclusions in minerals. Earth and Planetary Science Letters, 244, 683–694.

Holland, T.J.B. (1979) High water activities in the generation of high pressure kyanite eclogites of the Tauern Window, Austria. The Journal of Geology, 87, 1–27.

Holland, T., and Powell, R. (2011) An improved and extended internally consistent thermodynamic dataset for phases of petrological interest, involving a new equation of state for solids. Journal of Metamorphic Geology, 29, 333–383.

Holland, T.J.B., Redfern, S.A.T., and Pawley, A.R. (1996) Volume behavior of hydrous minerals at high pressure and temperature: II. Compressibilities of lawsonite, zoisite, clinozoisite, and epidote. American Mineralogist, 81, 341–348.

Hoschek, G. (2001) Thermobarometry of metasediments and metabasites from the Eclogite zone of the Hohe Tauern, Eastern Alps, Austria. Lithos, 59, 127–150.

——— (2007) Metamorphic peak conditions of eclogites in the Tauern Window, Eastern Alps, Austria: Thermobarometry of the assemblage garnet + omphacite + phengite + kyanite + quartz. Lithos, 93, 1–16.
Howell, D., Wood, I.G., Nestola, F., Nimis, P., and Nasdala, L. (2012) Inclusions under remnant pressure in diamond: a multi-technique approach. European Journal of Mineralogy, 24, 563–573.
Izraeli, E.S., Harris, J.W., and Navon, O. (1999) Raman barometry of diamond formation. Earth and Planetary Science Letters, 173, 351–360.
Kouketsu, Y., Enami, M., Mouri, T., Okamura, M., and Sakurai, T. (2014) Composite metamorphic history recorded in garnet porphyroblasts of Sambagawa metasediments in the Besshi region, central Shikoku, Southwest Japan. Island Arc, 23, 263–280.
Kueter, N., Soesilo, J., Fedortchouk, Y., Nestola, F., Belluco, L., Troch, J., Wälle, M., Guillong, M., Von Quadt, A., and Driesner, T. (2016) Tracing the depositional history of Kalimantan diamonds by zircon provenance and diamond morphology studies. Lithos, 265, 159–176.
Kurz, W., Neubauer, F., and Dachs, E. (1998) Eclogite meso- and microfabrics: implications for the burial and exhumation history of eclogites in the Tauern Window (Eastern Alps) from *P-T*-d paths. Tectonophysics, 285, 183–209.
Kuzmany, H. (2009) Solid-State Spectroscopy: An introduction. Springer Science and Business Media.
Lafuente, B., Downs, R.T., Yang, H., and Stone, N. (2016) The power of databases: the RRUFF project. In T. Armbruster and R.M. Danisi, Eds., Highlights in Mineralogical Crystallography, pp. 1–29. Walter de Gruyter GmbH.
Mao, Z., Jiang, F., and Duffy, T.S. (2007) Single-crystal elasticity of zoisite $Ca_2Al_3Si_3O_{12}$ (OH) by Brillouin scattering. American Mineralogist, 92, 570–576.
Mazzucchelli, M.L., Burnley, P., Angel, R.J., Morganti, S., Domeneghetti, M.C., Nestola, F., and Alvaro, M. (2018) Elastic geothermobarometry: Corrections for the geometry of the host-inclusion system. Geology, 46, 231–234.
Miller, C., and Konzett, J. (2003) Magnesiochloritoid-talc-garnet assemblages from the Tauern Window, Eastern Alps, Austria: High pressure metamorphosed oceanic hydrothermal veins p. 5206. Presented at the EGS AGU EUG Joint Assembly.
Murri, M., Mazzucchelli, M.L., Campomenosi, N., Korsakov, A.V., Prencipe, M., Mihailova, B.D., Scambelluri, M., Angel, R.J., and Alvaro, M. (2018) Raman elastic geobarometry for anisotropic mineral inclusions. American Mineralogist, 103, 1869–1872.
Murri, M., Alvaro, M., Angel, R.J., Prencipe, M., and Mihailova, B.D. (2019) The effects of non-hydrostatic stress on the structure and properties of alpha-quartz. Physics and Chemistry of Minerals.
Myer, G.H. (1965) X-ray determinative curve for epidote. American Journal of Science, 263, 78–86.
——— (1966) New data on zoisite and epidote. American Journal of Science, 264, 364–385.
Nestola, F., Nimis, P., Ziberna, L., Longo, M., Marzoli, A., Harris, J.W., Manghnani, M.H., and Fedortchouk, Y. (2011) First crystal-structure determination of olivine in diamond: Composition and implications for provenance in the Earth's mantle. Earth and Planetary Science Letters, 305, 249–255.
Nestola, F., Prencipe, M., Nimis, P., Sgreva, N., Perritt, S.H., Chinn, I.L., and Zaffiro, G. (2018) Toward a robust elastic geobarometry of kyanite inclusions in eclogitic diamonds. Journal of Geophysical Research: Solid Earth. DOI: 10.1029/2018JB016012
Nestola, F., Zaffiro, G., Mazzucchelli, M.L., Nimis, P., Andreozzi, G.B., Periotto, B., Princivalle, F., Lenaz, D., Secco, L., Pasqualetto, L., and others (2019) Diamond-inclusion system recording old deep lithosphere conditions at Udachnaya (Siberia). Scientific Reports, 9, 1–8.
Nye, J.F. (1985) Physical Properties of Crystals: Their representation by tensors and matrices. Oxford University Press.
Parkinson, C.D., and Katayama, I. (1999) Present-day ultrahigh-pressure conditions of coesite inclusions in zircon and garnet: Evidence from laser Raman microspectroscopy. Geology, 27, 979–982.
Pawley, A.R., Redfern, S.A.T., and Holland, T.J.B. (1996) Volume behavior of hydrous minerals at high pressure and temperature: I. Thermal expansion of lawsonite, zoisite, clinozoisite, and diaspore. American Mineralogist, 81, 335–340.
Peacock, S.M. (1993) The importance of blueschist → eclogite dehydration reactions in subducting oceanic crust. GSA Bulletin, 105, 684–694.
Qin, F., Wu, X., Wang, Y., Fan, D., Qin, S., Yang, K., Townsend, J.P., and Jacobsen, S.D. (2016) High-pressure behavior of natural single-crystal epidote and clinozoisite up to 40 GPa. Physics and Chemistry of Minerals, 43, 649–659.
Rubie, D.C. (1998) Disequilibrium during metamorphism: The role of nucleation kinetics. Geological Society, London, Special Publications, 138, 199–214.
Ryzhova, T.V., Aleksandrov, K.S., and Korobkova, V.M. (1966) The elastic properties of rock-forming minerals; *V*, Additional data on silicates. Physics of the Solid Earth, 2, 63–65.
Schmidt, C., and Ziemann, M.A. (2000) In-situ Raman spectroscopy of quartz: A pressure sensor for hydrothermal diamond-anvil cell experiments at elevated temperatures. American Mineralogist, 85, 1725–1734.
Selverstone, J. (1985) Petrologic constraints on imbrication, metamorphism, and uplift in the SW Tauern Window, eastern Alps. Tectonics, 4, 687–704.
Selverstone, J., and Sharp, Z.D. (2013) Chlorine isotope constraints on fluid-rock interactions during subduction and exhumation of the Zermatt-Saas ophiolite. Geochemistry, Geophysics, Geosystems, 14, 4370–4391.
Selverstone, J., and Spear, F.S. (1985) Metamorphic *P-T* paths from pelitic schists and greenstones from the south-west Tauern Window, Eastern Alps. Journal of Metamorphic Geology, 3, 439–465.
Selverstone, J., Franz, G., Thomas, S., and Getty, S. (1992) Fluid variability in 2 GPa eclogites as an indicator of fluid behavior during subduction. Contributions to Mineralogy and Petrology, 112, 341–357.
Sobolev, N.V., Fursenko, B.A., Goryainov, S.V., Shu, J., Hemley, R.J., Mao, H., and Boyd, F.R. (2000) Fossilized high pressure from the Earth's deep interior: The coesite-in-diamond barometer. Proceedings of the National Academy of Sciences, 97, 11875–11879.
Spear, F.S., and Franz, G. (1986) *P-T* evolution of metasediments from the Eclogite Zone, south-central Tauern Window, Austria. Lithos, 19, 219–234.
Spear, F.S., and Selverstone, J. (1983) Quantitative *P-T* paths from zoned minerals: Theory and tectonic applications. Contributions to Mineralogy and Petrology, 83, 348–357.
Spear, F.S., Thomas, J.B., and Hallett, B.W. (2014) Overstepping the garnet isograd: A comparison of QuiG barometry and thermodynamic modeling. Contributions to Mineralogy and Petrology, 168, 1059.
Thomas, J.B., and Spear, F.S. (2018) Experimental study of quartz inclusions in garnet at pressures up to 3.0 GPa: Evaluating validity of the quartz-in-garnet inclusion elastic thermobarometer. Contributions to Mineralogy and Petrology, 173, 42.
Turner, F.J. (1981) Metamorphic Petrology: Mineralogical, field, and tectonic aspects. Hemisphere Publishing Corporation.
van der Klauw, S.N.G.C., Reinecke, T., and Stöckhert, B. (1997) Exhumation of ultrahigh-pressure metamorphic oceanic crust from Lago di Cignana, Piemontese zone, western Alps: The structural record in metabasites. Lithos, 41, 79–102.
Wang, J., Mao, Z., Jiang, F., and Duffy, T.S. (2015) Elasticity of single-crystal quartz to 10 GPa. Physics and Chemistry of Minerals, 42, 203–212.
Zhong, X., Andersen, N.H., Dabrowski, M., and Jamtveit, B. (2019) Zircon and quartz inclusions in garnet used for complementary Raman thermobarometry: application to the Holsnøy eclogite, Bergen Arcs, Western Norway. Contributions to Mineralogy and Petrology, 174, 50.

Manuscript received May 13, 2019
Manuscript accepted February 2, 2020
Manuscript handled by Claudia Cannatelli

Endnote:

[1]Deposit item AM-20-87379, Supplemental Material. Deposit items are free to all readers and found on the MSA website, via the specific issue's Table of Contents (go to http://www.minsocam.org/MSA/AmMin/TOC/2020/Aug2020_data/Aug2020_data.html).